Article
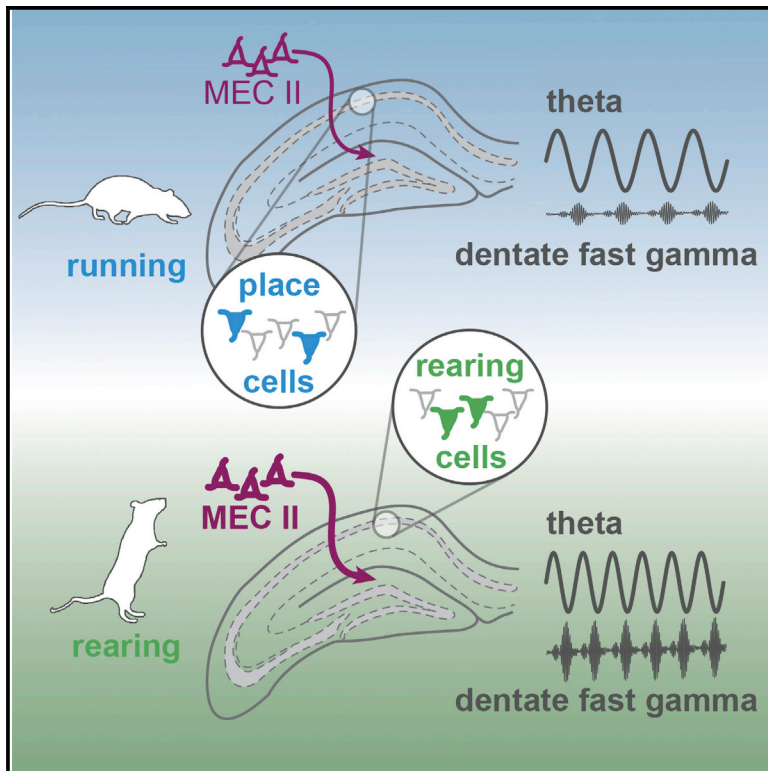
Hippocampal Network Dynamics during Rearing Episodes

Graphical Abstract

Authors

Albert M. Barth, Andor Domonkos,
Antonio Fernandez-Ruiz,
Tamas F. Freund, Viktor Varga

Correspondence

vargav@koki.mta.hu

In Brief

By combining high speed tracking in three dimensions and multichannel recording, Barth et al. characterize the network dynamics in the hippocampus during rearing episodes. They observe augmented impulse flow through the medial perforant pathway accompanied by the activation of certain principal cells and decrease of place cell activity.

Highlights

- Theta frequency increased during rearing coupled with an elevated dentate theta sink

- Robust theta-fast gamma phase coupling in the dentate gyrus accompanied rearing

- Rearing-specific firing rate increase of putative pyramidal cells was detected

- Conversely, if rearing occurred in a neuron's place field, its firing rate decreased

CellPress

Hippocampal Network Dynamics during Rearing Episodes

Albert M. Barth,[1] Andor Domonkos,[1] Antonio Fernandez-Ruiz,[2] Tamas F. Freund,[1] and Viktor Varga[1,2,3,*]

[1]Cerebral Cortex Research Group, Department of Cell and Network Neurobiology, Institute of Experimental Medicine of the Hungarian Academy of Sciences, Budapest 1083, Hungary
[2]Neuroscience Institute, School of Medicine, New York University, New York, NY 10016, USA
[3]Lead Contact
*Correspondence: vargav@koki.mta.hu
https://doi.org/10.1016/j.celrep.2018.04.021

SUMMARY

Animals build a model of their surroundings on the basis of information gathered during exploration. Rearing on the hindlimbs changes the vantage point of the animal, increasing the sampled area of the environment. This environmental knowledge is suggested to be integrated into a cognitive map stored by the hippocampus. Previous studies have found that damage to the hippocampus impairs rearing. Here, we characterize the operational state of the hippocampus during rearing episodes. We observe an increase of theta frequency paralleled by a sink in the dentate gyrus and a prominent theta-modulated fast gamma transient in the middle molecular layer. On the descending phase of rearing, a decrease of theta power is detected. Place cells stop firing during rearing, while a different subset of putative pyramidal cells is activated. Our results suggest that the hippocampus switches to a different operational state during rearing, possibly to update spatial representation with information from distant sources.

INTRODUCTION

When animals are exposed to novelty or experience alterations of a familiar environment, a complex set of behaviors unfolds. All of these behavioral actions aim to map the environment, and as such they are indispensable for the survival of the animal (O'Keefe and Nadel, 1979). A key component of this complex behavioral pattern is termed rearing and manifests as standing on the hindlimbs and scanning the environment from an elevated perspective (Lever et al., 2006). Changing the vantage point of the animal during exploration allows access to information from sources not immediately detectable during horizontal ambulation. Indeed, the occurrence of rearing is correlated with novelty, and can be used as a sensitive measure of exploratory behavior (Lever et al., 2006; Mun et al., 2015; Wells et al., 2013).

In addition to the spatial memory deficits, hippocampal damage impairs novelty detection and disrupts the normal pattern of rearing (Deacon et al., 2002; Harley and Martin, 1999). Rearing

deficits may occur because of failures in spatial memory, where the novelty detection is impaired, thus failing to elicit the relevant behaviors normally triggered in a new space. Spatial memory is thought to rely upon comparing sensory inputs with the hippocampal-dependent representation of familiar places. Such spatial representations are supported by hippocampal "place cells" that are spatially selective and fire during movement throughout an animal's environment (O'Keefe and Nadel, 1979; Wilson and McNaughton, 1993).

Place cell activity during exploration is organized by the 5–12 Hz theta rhythm as well as higher frequency gamma oscillations (Bragin et al., 1995; Buzsáki et al., 1983) that reflect local computations and dynamic changes of the information flow via hippocampal afferents (Colgin et al., 2009; Schomburg et al., 2014). Therefore, novelty-related behaviors may be triggered by, or in turn influence, place cell activity and the rhythms that coordinate the hippocampal system.

To address this question, we recorded hippocampal activity during rearing. We hypothesized that the information flow through the hippocampus would change when the animal changes its vantage point to switch from a focus on local cues to a focus on the more distant landmarks within an environment (Knierim and Hamilton, 2011). In the few studies that have examined the hippocampal electrophysiological correlates of rearing, robust theta was detected (Vanderwolf, 1969, 1975; Young and McNaughton, 2009). However, lack of appropriate tracking of the animal's position precluded sufficiently detailed analysis of rearing-specific hippocampal activity. We combined a high-speed, three-dimensional (3D) behavioral tracking system with electrophysiological recordings from multiple hippocampal subregions to uncover rearing-associated network and single unit dynamics.

RESULTS

Rearing Is Accompanied by Increased Hippocampal Theta Frequency

To investigate rearing behavior, mice (n = 12, both transgenic and wild-type; see Experimental Procedures; Table S1) were recorded during open-field exploration. Local field potentials (LFPs) and single units were registered across hippocampal subregions with multisite silicon probes, and the position of the animal was captured with simultaneous high-speed 3D behavioral tracking (Figure 1A). We defined rearing events on the basis of
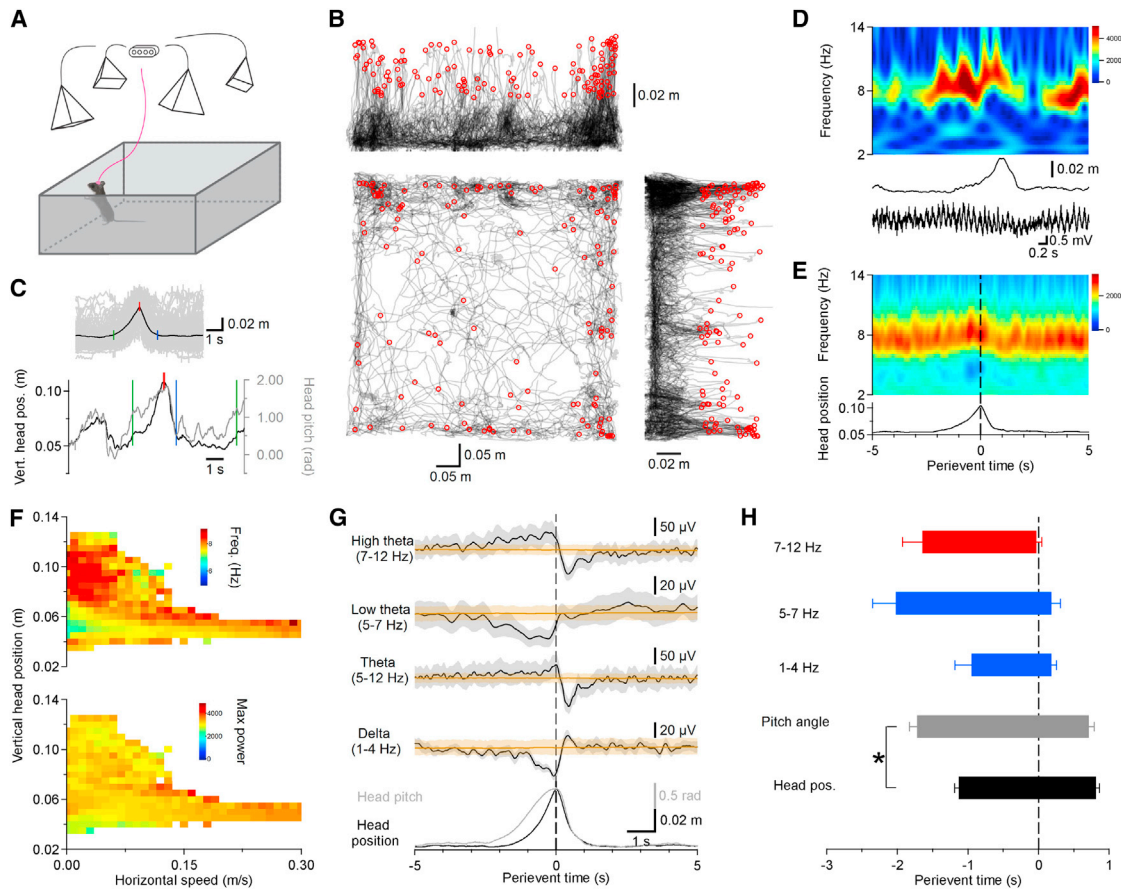
Figure 1. Rearing Events Are Accompanied by Theta Oscillation Alterations

(A) Arrangement of the 3D behavioral observation system. Four cameras recorded the position of markers on the mouse's head implant. The motion capture software reconstructed the exact position and orientation of the animal's head in real time.

(B) Sample trajectory from an animal in the open arena during one trial (top right, side views, bottom left, top view). Red circles indicate rearing events.

(C) Example rearing event: black, vertical head position; gray, head pitch angle; green vertical line, start; red vertical line, peak; blue vertical line, stop of rearing event. Inset shows the average of n = 132 rearing events of one animal in black; the overlaid individual events are in gray.

(D) Example LFP recording in the CA1 pyramidal cell layer (bottom trace) during one rearing episode (vertical head positions, middle trace) and corresponding wavelet spectrogram of the LFP (top). Note the elevated frequency of theta oscillation during the rearing event.

(E) Rearing peak-triggered average vertical head position (bottom) and the corresponding average wavelet spectrogram (top) of all rearing events of an animal.

(F) Theta oscillation frequency (top diagram) and power (bottom) as a function of running speed and vertical head position. Note the high theta frequency values at low running speed and high head position.

(G) Mean power in different frequency bands around rearing events calculated for all mice. A prominent increment of high theta power is paralleled by the reduction of low theta power. Brown traces indicate the shuffled control (n = 12 animals; shaded gray area corresponds to SEM; beige area represents the 99% band of the shuffled control).

(H) Timing of changes in the delta and theta bands during rearing. Horizontal bars indicate the duration of the LFP and behavioral events; error bars represent SEM. Red, power increment; blue, power reduction. Note that power alterations of high and low theta tended to precede the start of head lift-up but nearly coincided with change of pitch angle (*p < 0.05, paired t test; n = 12 animals).

See also Figure S1.

the distribution of vertical head positions (see Experimental Procedures; Figures S1A, 1B, and 1C). As expected (Lever et al., 2003; Mun et al., 2015), we found an initial surge in rearing during the first few minutes of an open-field test, followed by a gradual decrease (Figures S1B and S1C). Previous studies demonstrated a positive correlation between the frequency and power of theta oscillation and the animal's horizontal running speed (McFarland et al., 1975). Therefore, we investigated the dependence of theta frequency and power on horizontal speed as well as vertical head position. The frequency of theta recorded

in the dorsal CA1 pyramidal layer significantly increased during rearing episodes (Figures 1D–1G; −10 to −5 s before rearing peak 7.9 ± 0.1 Hz; −0.5 s to rearing peak 8.2 ± 0.1 Hz; $t_{[11]}$ = −4.73; p = 0.0006, paired t test; n = 12 mice). In addition to the known correlation between horizontal speed and theta frequency (Figure S1D; Pearson's r = 0.45, p = 0.0003, n = 12 mice) and power (Pearson's r = 0.51, p = 0.00003, n = 12 mice), our analysis also revealed high-frequency theta oscillations at elevated head positions, which typically occur during slow horizontal velocities (Figure 1F). The peak frequency during
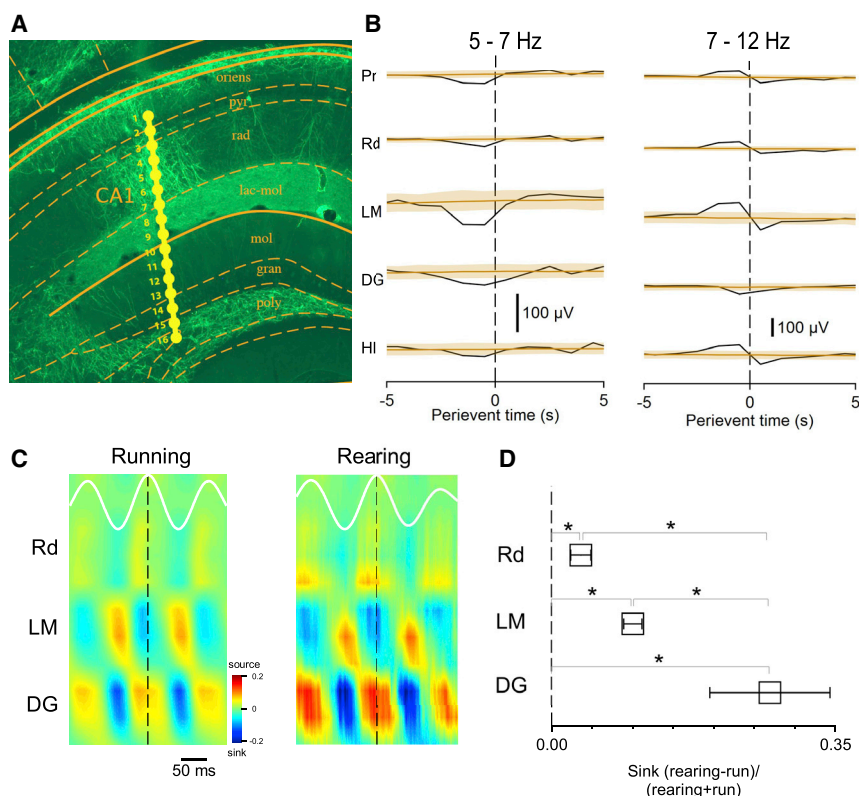
Figure 2. Enhancement of the DG Sink during Rearing

(A) Histological image shows the linear silicone probe track through all layers of the hippocampus. Oriens, stratum oriens; pyr, pyramidal layer; rad, radiatum; lac-mol, lacunosum-moleculare; mol, molecular layer; gran, granule cell layer; poly, polymorphic layer.

(B) Perievent binned (bin size = 1 s) average power in the low and high theta bands in the main layers of the hippocampal formation. Brown traces indicate the shuffled control (n = 4 animals; shaded area represents the 99% band of the shuffled control). Note the high theta power elevations in the lacunosum-moleculare and in the hilus of the DG.

(C) CSD maps from an animal of averaged LFP profile during running (left) and rearing (right). White traces at the top indicate theta oscillation in the pyramidal layer.

(D) Comparison of current sink magnitude during running and rearing (*p < 0.05, ANOVA with post hoc Dunnett's test; n = 4 animals; values are mean ± SEM). Note the prominent increase of dentate gyrus sink during rearing compared to running. Pr, pyramidal layer; Rd, radiatum; LM, lacunosum-moleculare; DG, dentate gyrus; Hl, hilus.

See also Figure S2.

rearing episodes, which occur almost exclusively in the absence of horizontal motion, was similar to the highest value detected during running (Figure S1D; 8.2 ± 0.1 Hz at 0.12 m/s running speed versus 8.2 ± 0.1 Hz during rearing; $t_{[11]} = -0.371$; p = 0.72, paired t test; n = 12 mice). We then asked if the rearing-coupled increase of theta frequency was correlated with vertical head position and the speed of movement along the vertical dimension. Cross-correlogram of vertical head position and high theta power indicated that increase of high theta power leads the elevation of vertical head position (Figure S1E; lag −0.43 ± 0.11 s; p = 0.0026, t test; n = 12 mice). Theta oscillation frequency and vertical head position showed a weak correlation, and the correlation at higher head positions had disappeared (Figure S1G; Pearson's r = 0.32, p = 0.002; above 0.03 m from baseline, Pearson's r = −0.04, p = 0.77; n = 12 animals). Because the horizontal and vertical components of 3D speed can be associated with different theta frequencies (Figure S1F), we used only its vertical component. We found that theta oscillation frequency correlated with vertical speed during both upward and downward movement (Figure S1H; Pearson's r for upward movement = 0.51, p = 1.1×10^{-7}; Pearson's r for downward movement = −0.28, p = 0.005; comparison of correlations by Fisher r-to-z transformation, z = 1.84, p = 0.07; n = 12 animals). We suppose that the decreasing vertical head speed and the correlated theta frequency reduction close to peak positions (Figure S1H, right) can explain the flattening of theta frequency and vertical head position correlation. Theta frequency had a tendency to increase coincident with the change in head pitch angle before the

elevation of vertical head position and continued accelerating during the lift-up of the body (Figures 1G and 1H). Although low-frequency (5–7 Hz) theta is typically observed in the absence of horizontal movement (Vanderwolf, 1969), during rearing we found an increase in high-frequency (7−12 Hz) theta (Figure 1G). These results suggest that rearing may be associated with a distinct brain state compared with that observed during running or immobility.

Increased Entorhinal-Driven Theta Currents during Rearing

Theta oscillation power and phase exhibit a characteristic depth profile across the layers of the hippocampal formation explained by the presence of different layer-specific theta current generators (Kocsis et al., 1999; Montgomery et al., 2009). Temporal shifts in the dominance of one theta generator over another can offer indirect insight into which afferent region is driving downstream activity on a moment-to-moment basis. Therefore, we investigated which theta current generators are involved in the observed theta oscillation alterations during rearing and hypothesized that rearing would be associated with an increased feedforward entorhinal drive due to the availability of new sensory inputs.

We used linear electrode arrays that spanned all CA1 layers and extended into the dentate gyrus to map layer-specific alterations during rearing episodes (Figure 2A). Similar to what we observed in the CA1 pyramidal cell layer, low-frequency theta was decreased and high-frequency theta was increased

throughout all of the sampled hippocampal layers with the exception of the dentate molecular layer (Figure 2B). To uncover the contribution of the major hippocampal theta generators during rearing, we performed current source density (CSD) analysis (Buzsáki et al., 1986) on LFPs recorded during rearing and running (horizontal speed above 4 cm/s) epochs. During running episodes, as reported earlier (Buzsáki et al., 1986; Brankačk et al., 1993), a large-magnitude sink at the peak of pyramidal layer theta oscillation was found in the stratum lacunosum-moleculare (the target domain of entorhinal layer III axons), accompanied by a phase-shifted sink in the dentate gyrus molecular layer (the target domain of entorhinal layer II terminals) and a weaker sink in CA1 stratum radiatum (the target domain of CA3 axons) (Figure 2C). Rearing episodes were characterized by moderate elevations of CA1 radiatum and lacunosum-moleculare sinks and a prominent increase of the dentate gyrus sink (Figures S2, 2C, and 2D; rearing-coupled change of sink values compared with running: radiatum sink $3.6\% \pm 1.3\%$, lacunosum-moleculare sink $10.0\% \pm 1.1\%$, dentate gyrus sink $26.8\% \pm 7.4\%$; dentate versus lacunosum-moleculare sink, $p = 0.02$; dentate versus radiatum sink, $p = 0.004$; $n = 4$ mice; ANOVA $F_{[2,9]} = 7.53$, $p = 0.012$ with post hoc Dunnett's test). This laminar pattern of current sinks implies that rearing is associated with increased entorhinal inputs through the dentate gyrus via the perforant pathway as well as a weaker entorhinal layer III input to CA1 through the temporoammonic pathway.

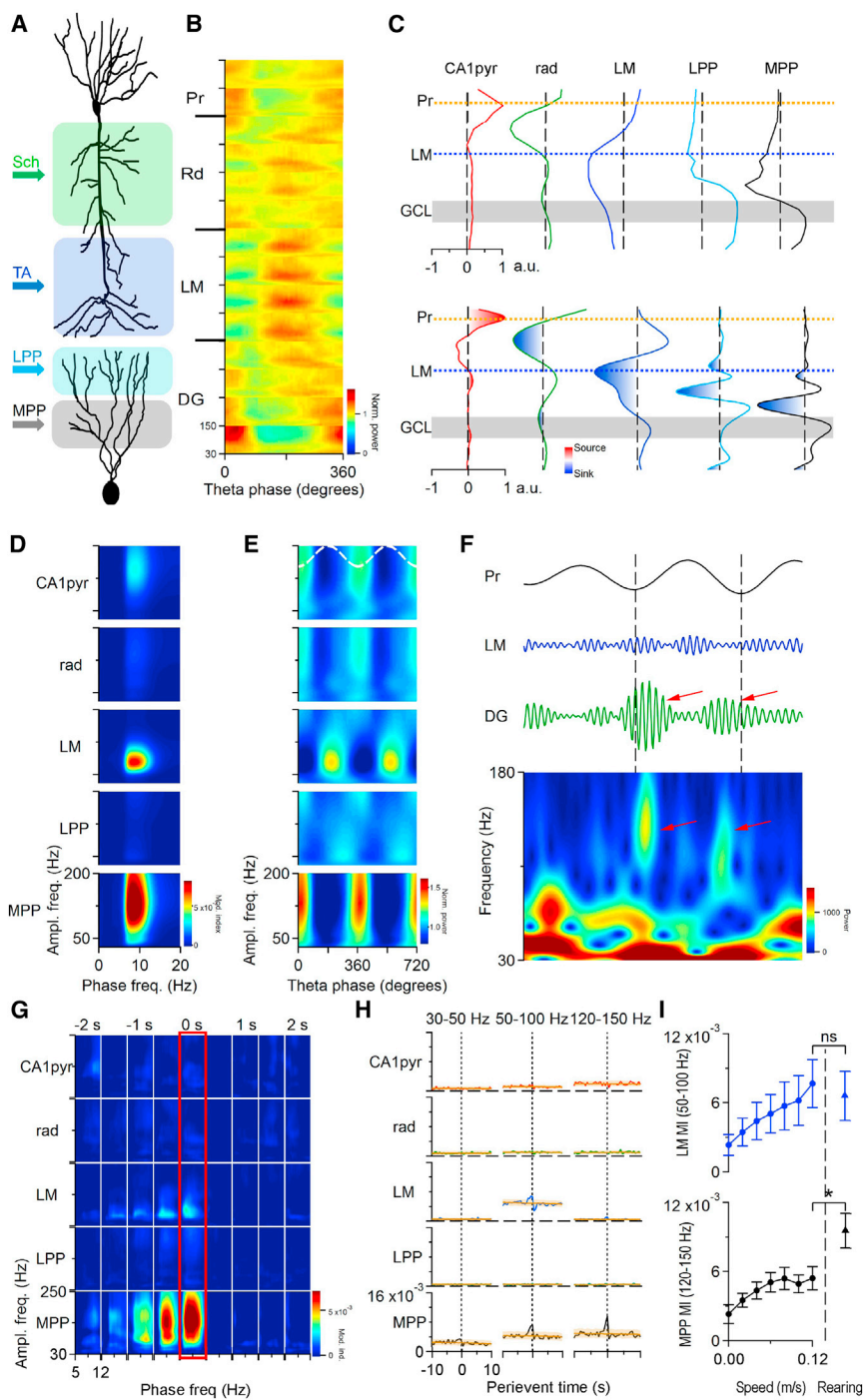## Theta-Gamma Coupling in the Dentate Gyrus during Rearing Episodes

Theta and gamma oscillations are tightly coupled throughout the hippocampal formation (Bragin et al., 1995; Colgin et al., 2009; Csicsvari et al., 2003). Recently, the different theta phase-coupled gamma oscillations have been linked to specific pathways in the hippocampal formation (Figure 3A) (Colgin et al., 2009; Fernández-Ruiz et al., 2017; Lasztóczi and Klausberger, 2017; Schomburg et al., 2014). Previous studies have separated three different gamma frequency bands in CA1 (slow 30–50 Hz, mid 50–100 Hz, fast 120–150 Hz; Belluscio et al., 2012; Schomburg et al., 2014) that are linked to different current generators (i.e., synaptic inputs) and coupled to different phases of ongoing theta oscillation (Figures 3A and 3B). Because LFPs recorded at any location in the hippocampus are a mixture of local and distant volume-conducted fields (Buzsáki et al., 2012), we sought to disentangle the distinct gamma generators by applying independent-component analysis (ICA) to wide gamma band LFPs (30–200 Hz) in CA1 and the dentate (Fernández-Ruiz and Herreras, 2013). In each animal, five main independent components (ICs) were separated and identified as previously described (Fernández-Ruiz and Herreras, 2013; Fernández-Ruiz et al., 2012; Schomburg et al., 2014). Each component showed characteristic voltage and CSD depth profiles corresponding to the anatomical location of the underlying current sources and sinks (Figure 3C). Three ICs had activity restricted to the CA1 region, in the pyramidal (*CA1pyr*), radiatum (*rad*), and lacunosum-moleculare (*LM*) layers, respectively (Figure 3C, columns 1–3). Previous work identified the synaptic origin of these current generators: CA1 local circuits (*CA1pyr*), CA3 input to CA1 through Schaffer collaterals (*rad*), and entorhinal layer III

input to CA1 through the temporoammonic pathway (*LM*) (Benito et al., 2014; Fernández-Ruiz et al., 2012, 2017; Schomburg et al., 2014). Two additional ICs were restricted to the dentate gyrus, with main currents in the outer third (*LPP*) and middle third (*MPP*) of the molecular layer (Fernández-Ruiz et al., 2013), the target dendritic regions of perforant pathway axons from lateral and medial entorhinal cortex respectively (Figure 3C, columns 4 and 5).

Having identified dissociable gamma generators, we next sought to link that pathway-specific activity with theta oscillations and rearing episodes. Previous studies have demonstrated that gamma oscillatory activity in the hippocampus is tightly modulated by theta phase, a phenomenon called cross-frequency phase-amplitude coupling (CFC) (Bragin et al., 1995; Colgin et al., 2009). Therefore, we calculated the theta phase-gamma amplitude comodulograms of the five ICs for running episodes by using CA1 pyramidal layer theta as a reference. Phase-amplitude comodulograms of the five ICs calculated for running epochs showed modulation in specific gamma sub-bands and preferred theta phases, corresponding to isolated layer-specific gamma oscillations (Figures 3D and 3E), in agreement with previous reports in both rats and mice (Fernández-Ruiz et al., 2017; Lasztóczi and Klausberger, 2016, 2017; Schomburg et al., 2014).

We hypothesized that alteration of the animal's vantage point and the resulting change in multimodal stimuli would lead to the redistribution of inputs and thus to the reorganization of theta-modulated gamma oscillations. Consistent with this view, theta-fast gamma coupling in the middle molecular layer of the dentate gyrus (*MPP* component) increased prominently during rearing (modulation index [MI] values of baseline 5–10 s before rearing peak versus rearing peak 0.0047 ± 0.00067 versus 0.0098 ± 0.0018; $t_{[4]} = -3.081$; $p = 0.037$, paired t test; $n = 5$ animals) and showed maximal theta phase coupling during peak vertical head positioning (Figures 3G, 3H, and S3). Importantly, this fast gamma was likely not due to contamination from multi-unit activity, as the cross-frequency coupling between fast gamma and high-frequency oscillations above 300 Hz was insignificant (Figure S3H). No other components exhibited significant rearing-coupled changes (*CA1pyr* fast gamma 0.0021 ± 0.00049 versus 0.0024 ± 0.00072, $t_{[4]} = -1.027$, $p = 0.36$; *rad* slow gamma 0.00087 ± 0.00031 versus 0.0011 ± 0.0005, $t_{[4]} = -0.729$, $p = 0.51$; *LM* mid gamma 0.005 ± 0.0019 versus 0.0066 ± 0.0026, $t_{[4]} = -2.038$, $p = 0.11$; *LPP* slow gamma 0.0005 ± 0.00009 versus 0.0007 ± 0.0003, $t_{[4]} = -0.855$, $p = 0.44$; paired t test; $n = 5$ animals). Note that the two strongest gamma components, *LM* and *MPP*, have opposite theta phase preferences (Figure 3E). Their preferred theta phase matches with the reported firing phase of entorhinal cortex layer III and layer II principal cells, respectively (Fernández-Ruiz et al., 2017; Mizuseki et al., 2009) and with the phase-shifted theta sinks in stratum lacunosum-moleculare and dentate (Figure 2C). These results suggest that during rearing episodes, medial entorhinal cortex (MEC) inputs to the hippocampus are enhanced, especially those originating in layer II (van Groen et al., 2003).

Running speed has been shown to modulate gamma amplitude in CA1 (Ahmed and Mehta, 2012; Zheng et al., 2015). However, the decoupling of theta frequency and speed of horizontal movement during rearing events raises the possibility of

Figure 3. Robust Enhancement of Theta-Gamma Coupling in the Dentate Gyrus during Rearing Events

(A) Anatomical sketch that depicts the main inputs of CA1 pyramidal and dentate granule cells. Sch, Schaffer; TA, temporoammonic; LPP, lateral perforant; MPP, medial perforant pathways.

(B) CSD wavelet spectrograms indicate the characteristic gamma bands and their theta phase along the hippocampal formation. Pr, pyramidal layer; Rd, radiatum; LM, lacunosum-moleculare; DG, dentate gyrus.

(C) Independent-component analysis (ICA) of hippocampal LFPs resulted in five main components (ICs), three restricted to the CA1 area and two to the dentate gyrus. Top row: voltage loadings of the five identified LFP generators in the hippocampal formation (from left to right: CA1pyr, CA1 pyramidal layer; rad, radiatum; LM, lacunosum-moleculare; LPP, lateral perforant path; MPP, medial performant path generators; from top to bottom: Pr, pyramidal layer; LM, lacunosum-moleculare; GCL, granule cell layer). Bottom row: CSD loadings of the same generators. In the dentate gyrus one component had maximal negative amplitude in the outer molecular layer (LPP) and the other (MPP) in the middle of it and both had positive polarity through the granular layer and the hilus.

(D) Average cross-frequency-amplitude comodulograms for the five ICs during running (averages of n = 5 animals).

(E) Average theta phase-gamma amplitude coupling matrices for the five ICs during running (averages of n = 5 animals). Two theta cycles are shown for visualization purposes. Top dashed trace indicates theta oscillation in the CA1 pyramidal layer. Note the opposite theta-phase preference of LM and MPP gamma oscillations, matching the phase distribution of entorhinal layer II and III spiking and local gamma oscillations (Fernández-Ruiz et al., 2017). (D) and (E) were calculated from IC segments during which the animal movement speed was above 0.04 m/s for at least 2 s.

(F) Fast gamma in the dentate gyrus. First row: filtered (5–12 Hz) CA1 pyramidal layer LFP; second row: 120–150 Hz filtered lacunosum-moleculare LFP; third row: 120–150 Hz filtered dentate gyrus LFP; bottom row: wavelet spectrogram of the dentate gyrus LFP. Red arrows highlight fast gamma transients on the dentate gyrus recordings and corresponding wavelet spectrogram. Vertical dashed lines indicate the pyramidal layer theta troughs. Fast gamma components were not detected in the lacunosum-moleculare LFP.

(G) Average comodulograms of the five ICs for different time intervals around rearing peak

(averages of n = 5 animals). Plots were constructed by averaging individual comodulograms from five animals followed by the subtraction of baseline (−10 to −5 s to rearing peak) comodulograms. Red rectangle highlights comodulograms at rearing peak (0 s). Note the robust enhancement of the theta coupling of the medial perforant path generator (MPP).

(H) Average perievent modulation index values of the five ICs (rows) in three different gamma frequency bands (columns; averages of n = 5 animals, brown traces indicate the shuffled control, shaded area represents the 99% band of the shuffled control). Vertical dashed lines at zero indicates rearing peak. The dentate fast gamma (MPP generator) has broad frequency range appearing in both 50–100 Hz and 120–150 Hz frequency bands.

(I) The coupling of LM mid gamma and MPP dentate fast gamma to theta oscillation increases with running speed. However, rearing-coupled MPP theta-gamma coupling is about two times larger than that is observed during running (*p < 0.05, paired t test; n = 5 animals; values are mean ± SEM).

See also Figure S3.

dissociation between horizontal movement and theta-modulated gamma patterns. Therefore, we determined the relationship between running and rearing-coupled dynamics of theta phase-gamma amplitude CFC. First, we found that theta-lacunosum-moleculare mid gamma CFC increased linearly with running speed (*LM*; Figures 3I, S3E, and S3G; for speed > 0.04 m/s: Pearson's r > 0.6, p < 0.005; n = 5 animals), in agreement with previous reports (Chen et al., 2011). In contrast, theta-dentate fast gamma (*MPP*) coupling and speed were not correlated (Figure 3I; for speed > 0.04 m/s: Pearson's r < 0.3, p > 0.1; n = 5 animals). The theta-lacunosum-moleculare mid gamma CFC during rearing did not surpass values that characterized high running speeds, whereas an almost 2-fold elevation was uncovered for the theta-dentate fast gamma coupling at the peak of rearing versus running (Figure 3I; *LM* IC 50–100 Hz CFC at rearing versus running at 0.12 m/s 81.15% $\pm$ 11.96%, $t_{[4]}$ = −1.577, p = 0.19; *MPP* IC 120–150 Hz CFC at rearing versus running at 0.12 m/s 190.28% $\pm$ 32.18%, $t_{[4]}$ = 2.805, p < 0.05; n = 5 animals). The above results regarding theta-gamma CFC during rearing compared with running were verified by both LFP and CSD analyses (Figures S3E and S3G). Taken together, the reorganization of theta-gamma patterns point to the redistribution of network activity both in hippocampal circuits and in input pathways dominated by an enhanced theta-gamma input from MEC to dentate gyrus (DG).

A Subpopulation of Hippocampal Units Shows Rearing-Coupled Facilitation

The analysis on network oscillations suggests a redistribution of inputs during rearing. Such redistribution may also affect neuronal firing dynamics, resulting in rearing-specific activity patterns of hippocampal units. To test this hypothesis, we next analyzed how single neurons respond during rearing epochs. On the basis of waveform features and firing rates, pyramidal layer single units were separated into putative interneurons and principal cells (Figures S4A and S4B; n = 124 putative pyramidal cells and n = 25 putative interneurons from n = 5 mice). Rearing peak-triggered firing histograms uncovered hippocampal principal units that showed robust firing rate increases around the rearing peak (rearing-on units, n = 11 from five animals; Figure 4A). The analysis of individual rearing events revealed that rearing-on units were activated in 27.5% $\pm$ 4.1% of rearing epochs (on average there were 20 $\pm$ 7 "active" rearing events for each rearing-on unit). We compared the spatial distribution of these "active" rearing events with randomly selected rearing events. For each rearing-on unit, the mean difference of horizontal positions of the "active" rearing events was calculated (see Experimental Procedures). We found no significant difference when we compared these values with randomized ones (average mean difference values for rearing-on units 0.20 $\pm$ 0.022 m, randomized 0.23 $\pm$ 0.007 m; n = 11; W = 20; p = 0.28, Wilcoxon signed-rank test). This calculation indicates that the "active" rearing events did not occur in a spatially restricted area. The comparison of the durations of the active and non-active rearing events did not reveal significant differences (duration of active versus non-active rearing episodes 2.08 $\pm$ 0.51 versus 2.06 $\pm$ 0.42 s; $t_{[10]}$ = 0.097; n = 11; p = 0.92, paired t test). We

also compared rearing events occurring at the periphery (within 5 cm of the walls) or in the center (beyond 5 cm from the wall). On average 84.3% $\pm$ 4% of the total rearing numbers occurred within 5 cm of a wall. Active rearing events were also observed at larger percentage at the periphery (periphery versus center 30.0% $\pm$ 4.6% versus 17.3% $\pm$ 5.5%; n = 9 rearing-on units; W = 3; p = 0.02, Wilcoxon signed-rank test). The higher incidence of rearing-on spiking near the walls indicated an apparent border preference of these units. However, this might be explained by the larger number of wall-proximal compared with central rearing events (Figures S4D and S4E). The acquisition of visual information is a key function of rearing, and visually guided directional tuning of hippocampal neuronal activity has recently been described (Acharya et al., 2016), so we tested if rearing-on units exhibit head directional preference. Because "behavioral constrains" (i.e., close to the wall, the mice preferentially head toward the wall) can result in apparent directional preference, we weighted the head direction distributions in each location bin by the firing rate of rearing-on units in that bin and calculated the correlation between the observed and reconstructed (weighted) head direction curves (Muller et al., 1994; Rubin et al., 2014). The reconstructed and observed head directions of rearing-on units were highly correlated, suggesting that instead of real head directional preference, behavioral constraints (i.e., proximity to the wall) could explain their apparent head direction tuning (Figure S4F). Finally, we found that rearing-on units showed a significant decrease in firing during movement (Figure 4G; firing rate during rearing 3.2 $\pm$ 0.8 Hz, during movement 0.6 $\pm$ 0.2 Hz; n = 11 rearing-on units in five mice; W = 5; p = 0.01, Wilcoxon signed-rank test).

In order to determine if rearing-on units correspond to a separate functional subgroup among hippocampal cells, we compared their activity with that of place cells. We identified place cells (see Experimental Procedures) and separated "infield" and "outfield" rearing events on the basis of whether the rearing occurred inside or outside the unit's place field (Figures 4B and 4C). Surprisingly, the activity of place cells was significantly decreased during rearing epochs, especially when the animal reared within the place cell's place field (Figures 4E–4G; infield firing rate during rearing 2.5 $\pm$ 0.4 Hz, during running 5.5 $\pm$ 0.5 Hz W = 120, p < 0.001; outfield firing rate during rearing 1.1 $\pm$ 0.2 Hz, during running 1.4 $\pm$ 0.2 Hz, n = 48 place cells in five mice, W = 220, p < 0.001 [Wilcoxon signed-rank test]). The decrease in the place cells' firing rate in a 0.5 s time window around rearing peaks was significantly higher when the rearing occurred infield versus outfield (percentage decrease of firing rate infield 46.3% $\pm$ 10.5% versus outfield 25.9% $\pm$ 5.7%; n = 48 place cells; p < 0.001, Wilcoxon signed-rank test). To further differentiate between rearing-on units and place cells, we calculated the distributions of vertical head positions and horizontal speed values corresponding to each spike. The average distributions show strikingly different patterns: place cells preferentially fire at "low" head positions (below rearing threshold), whereas rearing-on units fire at elevated head positions (Figure 4D; average head position from rearing threshold for rearing-on units 0.014 $\pm$ 0.003 m, n = 11; place cells −0.005 $\pm$ 0.001 m, n = 57; U = 47; p < 0.001, Wilcoxon-Mann-Whitney test). On average, rearing-on units also show lower
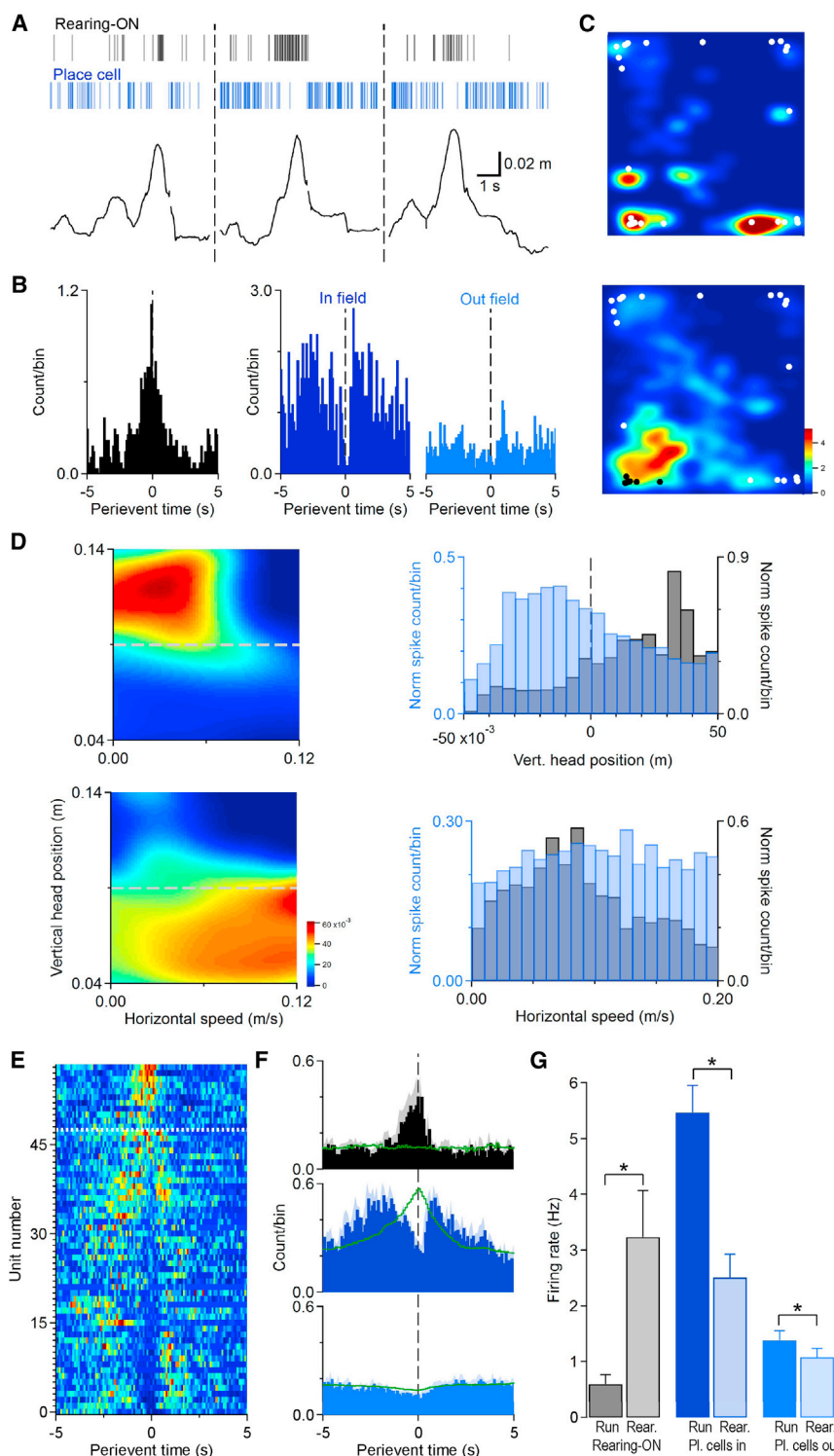
Figure 4. Single-Unit Activity during Rearing Behavior

(A) Rearing-on units and place cells show contrasting rearing-dependent activity. Bottom row: vertical head position during rearing events. Middle row: blue vertical lines, sample place cell spikes. Top row: black vertical lines, sample rearing-on unit spikes. The rearing-on unit increased and the place cell decreased activity during rearing epochs.

(B) Rearing peak-triggered perievent firing histograms corresponding to the units in A. Left: rearing-on unit; middle: place cell infield (within place field); right: place cell outfield (out of place field).

(C) Spatial firing maps of a rearing-on (top) and place cell (bottom, black dots indicate the infield, white dots the outfield rearing events).

(D) Rearing-on units and place cells have different firing preference for vertical head position and horizontal speed. Two-dimensional histograms show the horizontal speed and vertical head position dependence of a rearing-on unit (left top) and a place cell (left bottom). Units are the same as in (C). Horizontal gray dashed lines mark the threshold of rearing events. Average vertical head position (right top, overlaid histograms) and horizontal speed distributions (right bottom, overlaid histograms) highlight the differences between rearing-on units (gray) and place cells (blue). Vertical head positions are measured form the rearing threshold.

(E) Rearing peak-triggered perievent firing histograms of rearing-on units (above horizontal dashed line) and infield perievent histograms for place cells (below horizontal dashed line). The Z-scored perievent histograms were ordered by their average value between −0.25 and +0.25 s around rearing peaks.

(F) Average rearing peak-triggered perievent histograms of rearing-on units and place cells: rearing-on units (top; n = 11 units), place cells infield (middle; n = 48 units), place cells outfield (bottom; n = 48 units). Green traces indicate the shuffled data. Shaded area around the histogram bars corresponds to SEM.

(G) Summarized data showing the firing rate during running and rearing for rearing-on units and place cells. In the case of place cells, infield and outfield firing data are shown separately (*p < 0.05, Wilcoxon signed-rank test; n = 11 rearing-on units, n = 48 place cells; error bars represent SEM).

See also Figure S4.

2.06 ± 0.35 bits/spike, n = 11 units; for place cells 2.02 ± 0.16 bits/spike, n = 57 units; U = 307; p = 0.92, Wilcoxon-Mann-Whitney test; sparsity for rearing-on units 0.21 ± 0.03, n = 11 units; for place cells 0.26 ± 0.02, n = 57 units; U = 305; p = 0.89, Wilcoxon-Mann-Whitney

horizontal speed preference (Figure 4D; average horizontal speed values for rearing-on units 0.098 ± 0.006 m/s, n = 11 cells; place cells 0.117 ± 0.002 m/s, n = 57 cells; U = 142; p = 0.003, Wilcoxon-Mann-Whitney test). However, on the basis of conventional place cell metrics (spatial information for rearing-on units test), rearing-on units and place cells formed overlapping groups (n = 8 of 11 rearing-on units satisfied the criteria for place cells).

It has recently been reported that pyramidal cells in the CA2 area of the hippocampus show increased firing during immobility or low running speed, and these cells either decrease their activity

during sharp wave ripples or increase their firing right before them (Kay et al., 2016; Oliva et al., 2016). However, the robust elevation of rearing-on units firing rate at sharp wave ripple peaks (Figure S4C) distinguishes them from the immobility-related units described previously. Additionally, our histological reconstruction of electrode tracks verified that recordings were never performed close to the CA2 region. However, we cannot exclude a possible partial overlap between the recently characterized immobility-associated place cells in the CA1 and rearing-on units, though the former cells were mostly active near reward zones (Yu et al., 2017), whereas studying the reward-related activity of rearing-on units was beyond the scope of our study. In our experiments, we recorded free exploration without delivering reward, so comparison of data from the cited report with ours is not possible.

DISCUSSION

Using a combination of high-speed motion tracking in three dimensions and the recording of activity in multiple layers and subregions, we identified and characterized hippocampal network dynamics while mice were rearing on hindlimbs. During rearing, we found an increase in power of high-frequency theta across multiple hippocampal subregions. We also found an increase in theta phase-fast gamma amplitude coupling in the DG middle molecular layer, as well as an insignificant increase in theta-mid gamma coupling in the stratum lacunosum-moleculare. This theta-phase-modulated gamma amplitude is consistent with an increased flow of information from the entorhinal cortex (Fernández-Ruiz et al., 2017; Lasztóczi and Klausberger, 2017; Schomburg et al., 2014), with strong MEC layer II signaling to the DG and relatively moderate MEC layer III signaling to CA1. Finally, we observed different populations of pyramidal cells that were spatially tuned during running and decreased their activity during rearing ("place cells") and a different population that increased firing during rearing and showed reduced activity while the animal was running ("rearing-on units"). Such behavioral modulation of single cell activity suggests that the switch in afferent drive during rearing is sufficient to impose different processing modes on the hippocampus.

A prime function of rearing is to make alternative sources of multimodal sensory information (i.e., context) accessible for the exploring animal. In turn, the acquired information enables the recognition of novelty, the discrimination of different environments and ultimately, the refinement of the forming spatial map. DG is important for novelty-induced rearing and for learning new spatial information (Saab et al., 2009). In our study, the DG was found to be the main locus of rearing-coupled change of input patterns, suggesting that contextual information sampled during rearing events is conveyed mainly by the medial perforant pathway to the hippocampal formation through the DG (Kitamura et al., 2015). Our results may also support the possibility that rearing can contribute to the correction of position estimation. Navigation is known to be controlled by self-motion cues and distal landmark information (Etienne and Jeffery, 2004). Depriving the navigating animal from external cues leads to the accumulation of errors in the estimation of position (Séguinot et al., 1993). Visual input is thus crucial for correcting the positional signal (Maaswinkel and Whishaw, 1999) and rearing may be a critical moment

when such information is used to calibrate the cognitive map. Notably, without visually detectable external cues, the characteristic hexagonal grid pattern of activity in the MEC is also disrupted (Chen et al., 2016), possibly contributing to the deterioration of hippocampal position estimation. Therefore, increased input from the MEC to the DG in the rearing state implies that the information acquired during rearing can be pivotal for realigning the spatial map in the MEC as well as for updating the hippocampal spatial representation (Chen et al., 2016; Pérez-Escobar et al., 2016). In support of this role for rearing in reorganization of the cognitive map, new place fields often emerge in the locations in which rats stop and scan their environment (Monaco et al., 2014).

Hippocampal pyramidal cells can be tuned for multiple types of information (Wood et al., 2000). Rearing-on units were only activated in about a third of rearing events, suggesting that their activity is not representing the behavioral act of rearing but rather the specific information afforded by the change in vantage point. It is possible that the rearing-on units formed an unidentified subgroup of pyramidal cells, perhaps defined by the pattern of afferent connectivity. Alternatively, rearing-on cells could be activated by the altered neuromodulatory tone or by unreliable feedback from the motor system. We observed a slight preference of rearing-on unit activation for rearing events close to the walls of the arena, possibly reflecting a modulatory influence by boundary vector cells (Lever et al., 2009). Importantly, the lack of firing during ambulation of rearing-on units clearly differentiate them from other spatially modulated neurons of the hippocampal formation e.g., border cells (Solstad et al., 2008), grid cells (Hafting et al., 2005), or place cells (O'Keefe and Dostrovsky, 1971). However, the partial overlap of the rearing-on and place cell groups raises the possibility that the former neurons can be a subgroup of place cells, but it also highlights the limitations of determining the spatial correlates of activity without tracking the behavior in all three dimensions.

In contrast to rearing-on units, place cells exhibited decreased activity when rearing events occurred within their place fields. Reduction of firing can be caused by an active inhibitory process or can be due to the tuning of place cells' activity for representing location on the horizontal plane only during movement. Because of the firing rate reduction, the coding of the rearing-coupled location may be temporarily segregated from the code carried by typical "place cells." We hypothesize that rearing events may be triggered by moments of uncertainty about allocentric positioning, times when the cognitive map would contain the highest error and could most benefit from sensory driven re-alignment. Intra-place field reduction of place cell firing temporarily decouples the activity of place cells from that of rearing-related inputs. Thus, rearing can anchor the forming map to external cues and prevent the formation of erroneous associations between the cognitive map that has drifted and incoming perceptual inputs. Taken together, the rearing state may aid in the formation of a reliable map of the environment by allowing the repeated updating and correction of the spatial code during exploration.

EXPERIMENTAL PROCEDURES

Further details on the methods can be found in Supplemental Experimental Procedures.

Mice

Twelve male mice (two Vglut3-ires-Cre, seven Som-ires-Cre, one Vgat-ires-Cre, and two wild-type C57BL/6J, 2–5 months old) were used in this study (Table S1). All mice were used in other projects as well. Mice were kept in the vivarium on a 12 hr light/dark cycle and provided with food and water *ad libitum*. The animals were housed two or three per cage before surgery and individually after it. All experiments were approved by the Ethical Committee for Animal Research at the Institute of Experimental Medicine, Hungarian Academy of Sciences, and conformed to Hungarian (1998/XXVIII Law on Animal Welfare) and European Communities Council Directive recommendations for the care and use of laboratory animals (2010/63/EU) (license number PE/EA/2552-6/2016).

Summary of Methods

Details on the methods can be found in Supplemental Experimental Procedures. Briefly, mice were implanted with silicone probes targeting the dorsal hippocampus. Hippocampal activity was recorded while the animals were freely exploring a rectangular arena. Simultaneously with electrophysiological recording, the animals' movement was tracked in three dimensions using a multi-camera system. At the end of the experiments, mice were transcardially perfused, the brains were removed and sectioned, and the probe tracks were reconstructed. Rearing episodes were detected on the basis of the distribution of vertical head positions. Hippocampal LFP oscillations (delta, theta, and gamma) were separated using the time-frequency decomposition of the wide band LFP signal by continuous wavelet transformation or on the basis of the Hilbert magnitude of the band-pass-filtered signal (ripple). The relationship of hippocampal oscillations to rearing events was analyzed by peri-rearing distribution of power. The underlying current generators of theta and gamma oscillations were separated and analyzed by CSD and independent-component analyses. Theta-gamma cross-frequency coupling was calculated by using the phase of theta extracted from time-frequency decomposition and power, CSD, or separated ICs of gamma. Multiple single units were separated by principal-component analysis combined with clustering or by a template matching algorithm. Final spike clusters were generated by manual curation. The correlation of putative single units and rearing events was analyzed by perievent distribution of spikes. Various parameters (state-dependent firing rates, spatial information, sparsity, head direction tuning) of units that exhibited rearing-related and/or spatially modulated firing were calculated.

Quantification and Statistical Analysis

All statistical analyses were performed with standard IgorPro7 and MATLAB functions. For two-sample comparisons, the parametric Student's t test, non-parametric Wilcoxon signed-rank test, or Wilcoxon-Mann-Whitney test was used. For multiple comparisons, ANOVA with Tukey's honest significant difference or Dunnett's post hoc test was used. In the case of parametric statistics, normality was tested using the Shapiro-Wilk test, and equality of variances was tested using the F test or Levene's test. All graphs indicate mean $\pm$ SEM; n represents animal number or unit number as indicated. For significance, p = 0.05 was used.

SUPPLEMENTAL INFORMATION

Supplemental Information includes Supplemental Experimental Procedures, four figures, and one table and can be found with this article online at https://doi.org/10.1016/j.celrep.2018.04.021.

DECLARATION OF INTERESTS

The authors declare no competing interests.

REFERENCES

Acharya, L., Aghajan, Z.M., Vuong, C., Moore, J.J., and Mehta, M.R. (2016). Causal influence of visual cues on hippocampal directional selectivity. Cell *164*, 197–207.

Ahmed, O.J., and Mehta, M.R. (2012). Running speed alters the frequency of hippocampal gamma oscillations. J. Neurosci. *32*, 7373–7383.

Belluscio, M.A., Mizuseki, K., Schmidt, R., Kempter, R., and Buzsáki, G. (2012). Cross-frequency phase-phase coupling between θ and γ oscillations in the hippocampus. J. Neurosci. *32*, 423–435.

Benito, N., Fernández-Ruiz, A., Makarov, V.A., Makarova, J., Korovaichuk, A., and Herreras, O. (2014). Spatial modules of coherent activity in pathway-specific LFPs in the hippocampus reflect topology and different modes of presynaptic synchronization. Cereb. Cortex *24*, 1738–1752.

Bragin, A., Jandó, G., Nádasdy, Z., Hetke, J., Wise, K., and Buzsáki, G. (1995). Gamma (40-100 Hz) oscillation in the hippocampus of the behaving rat. J. Neurosci. *15*, 47–60.

Brankačk, J., Stewart, M., and Fox, S.E. (1993). Current source density analysis of the hippocampal theta rhythm: associated sustained potentials and candidate synaptic generators. Brain Res. *615*, 310–327.

Buzsáki, G., Leung, L.W., and Vanderwolf, C.H. (1983). Cellular bases of hippocampal EEG in the behaving rat. Brain Res. *287*, 139–171.

Buzsáki, G., Czopf, J., Kondákor, I., and Kellényi, L. (1986). Laminar distribution of hippocampal rhythmic slow activity (RSA) in the behaving rat: current-source density analysis, effects of urethane and atropine. Brain Res. *365*, 125–137.

Buzsáki, G., Anastassiou, C.A., and Koch, C. (2012). The origin of extracellular fields and currents—EEG, ECoG, LFP and spikes. Nat. Rev. Neurosci. *13*, 407–420.

Chen, Z., Resnik, E., McFarland, J.M., Sakmann, B., and Mehta, M.R. (2011). Speed controls the amplitude and timing of the hippocampal gamma rhythm. PLoS ONE *6*, e21408.

Chen, G., Manson, D., Cacucci, F., and Wills, T.J. (2016). Absence of visual input results in the disruption of grid cell firing in the mouse. Curr. Biol. *26*, 2335–2342.

Colgin, L.L., Denninger, T., Fyhn, M., Hafting, T., Bonnevie, T., Jensen, O., Moser, M.-B., and Moser, E.I. (2009). Frequency of gamma oscillations routes flow of information in the hippocampus. Nature *462*, 353–357.

Csicsvari, J., Jamieson, B., Wise, K.D., and Buzsáki, G. (2003). Mechanisms of gamma oscillations in the hippocampus of the behaving rat. Neuron *37*, 311–322.

Deacon, R.M.J., Croucher, A., and Rawlins, J.N.P. (2002). Hippocampal cyto-toxic lesion effects on species-typical behaviours in mice. Behav. Brain Res. *132*, 203–213.

Etienne, A.S., and Jeffery, K.J. (2004). Path integration in mammals. Hippocampus *14*, 180–192.

Fernández-Ruiz, A., and Herreras, O. (2013). Identifying the synaptic origin of ongoing neuronal oscillations through spatial discrimination of electric fields. Front. Comput. Neurosci. *7*, 5.

Fernández-Ruiz, A., Makarov, V.A., and Herreras, O. (2012). Sustained increase of spontaneous input and spike transfer in the CA3-CA1 pathway following long-term potentiation in vivo. Front. Neural Circuits *6*, 71.

Fernández-Ruiz, A., Muñoz, S., Sancho, M., Makarova, J., Makarov, V.A., and Herreras, O. (2013). Cytoarchitectonic and dynamic origins of giant positive local field potentials in the dentate gyrus. J. Neurosci. *33*, 15518–15532.

Fernández-Ruiz, A., Oliva, A., Nagy, G.A., Maurer, A.P., Berényi, A., and Buzsáki, G. (2017). Entorhinal-CA3 dual-input control of spike timing in the hippocampus by theta-gamma coupling. Neuron *93*, 1213–1226.e5.

Hafting, T., Fyhn, M., Molden, S., Moser, M.B., and Moser, E.I. (2005). Microstructure of a spatial map in the entorhinal cortex. Nature *436*, 801–806.

Harley, C.W., and Martin, G.M. (1999). Open field motor patterns and object marking, but not object sniffing, are altered by ibotenate lesions of the hippocampus. Neurobiol. Learn. Mem. *72*, 202–214.

Kay, K., Sosa, M., Chung, J.E., Karlsson, M.P., Larkin, M.C., and Frank, L.M. (2016). A hippocampal network for spatial coding during immobility and sleep. Nature *531*, 185–190.

Kitamura, T., Sun, C., Martin, J., Kitch, L.J., Schnitzer, M.J., and Tonegawa, S. (2015). Entorhinal cortical ocean cells encode specific contexts and drive context-specific fear memory. Neuron *87*, 1317–1331.

Knierim, J.J., and Hamilton, D.A. (2011). Framing spatial cognition: neural representations of proximal and distal frames of reference and their roles in navigation. Physiol. Rev. *91*, 1245–1279.

Kocsis, B., Bragin, A., and Buzsáki, G. (1999). Interdependence of multiple theta generators in the hippocampus: a partial coherence analysis. J. Neurosci. *19*, 6200–6212.

Lasztóczi, B., and Klausberger, T. (2016). Hippocampal place cells couple to three different gamma oscillations during place field traversal. Neuron *91*, 34–40.

Lasztóczi, B., and Klausberger, T. (2017). Distinct gamma oscillations in the distal dendritic fields of the dentate gyrus and the CA1 area of mouse hippocampus. Brain Struct. Funct. *222*, 3355–3365.

Lever, C., Cacucci, F., Wills, T., Burton, S., McClelland, J., Burgess, N., and O'Keefe, J. (2003). Spatial coding in the hippocampal formation: input, information type, plasticity, and behaviour. In The Neurobiology of Spatial Behavior, K.J. Jeffery, ed. (Oxford University Press).

Lever, C., Burton, S., and O'Keefe, J. (2006). Rearing on hind legs, environmental novelty, and the hippocampal formation. Rev. Neurosci. *17*, 111–133.

Lever, C., Burton, S., Jeewajee, A., O'Keefe, J., and Burgess, N. (2009). Boundary vector cells in the subiculum of the hippocampal formation. J Neurosci. *29*, 9771–9777.

Maaswinkel, H., and Whishaw, I.Q. (1999). Homing with locale, taxon, and dead reckoning strategies by foraging rats: sensory hierarchy in spatial navigation. Behav. Brain Res. *99*, 143–152.

McFarland, W.L., Teitelbaum, H., and Hedges, E.K. (1975). Relationship between hippocampal theta activity and running speed in the rat. J. Comp. Physiol. Psychol. *88*, 324–328.

Mizuseki, K., Sirota, A., Pastalkova, E., and Buzsáki, G. (2009). Theta oscillations provide temporal windows for local circuit computation in the entorhinal-hippocampal loop. Neuron *64*, 267–280.

Monaco, J.D., Rao, G., Roth, E.D., and Knierim, J.J. (2014). Attentive scanning behavior drives one-trial potentiation of hippocampal place fields. Nat. Neurosci. *17*, 725–731.

Montgomery, S.M., Betancur, M.I., and Buzsáki, G. (2009). Behavior-dependent coordination of multiple theta dipoles in the hippocampus. J. Neurosci. *29*, 1381–1394.

Muller, R.U., Bostock, E., Taube, J.S., and Kubie, J.L. (1994). On the directional firing properties of hippocampal place cells. J. Neurosci. *14*, 7235–7251.

Mun, H.S., Saab, B.J., Ng, E., McGirr, A., Lipina, T.V., Gondo, Y., Georgiou, J., and Roder, J.C. (2015). Self-directed exploration provides a Ncs1-dependent learning bonus. Sci. Rep. *5*, 17697.

O'Keefe, J., and Dostrovsky, J. (1971). The hippocampus as a spatial map. Preliminary evidence from unit activity in the freely-moving rat. Brain Res. *34*, 171–175.

O'Keefe, J., and Nadel, L. (1979). Précis of O'Keefe & Nadel's The hippocampus as a cognitive map. Behav. Brain Sci. *2*, 487–494.

Oliva, A., Fernández-Ruiz, A., Buzsáki, G., and Berényi, A. (2016). Role of hippocampal CA2 region in triggering sharp-wave ripples. Neuron *91*, 1342–1355.

Pérez-Escobar, J.A., Kornienko, O., Latuske, P., Kohler, L., and Allen, K. (2016). Visual landmarks sharpen grid cell metric and confer context specificity to neurons of the medial entorhinal cortex. eLife *5*, 5.

Rubin, A., Yartsev, M.M., and Ulanovsky, N. (2014). Encoding of head direction by hippocampal place cells in bats. J. Neurosci. *34*, 1067–1080.

Saab, B.J., Georgiou, J., Nath, A., Lee, F.J.S., Wang, M., Michalon, A., Liu, F., Mansuy, I.M., and Roder, J.C. (2009). NCS-1 in the dentate gyrus promotes exploration, synaptic plasticity, and rapid acquisition of spatial memory. Neuron *63*, 643–656.

Schomburg, E.W., Fernández-Ruiz, A., Mizuseki, K., Berényi, A., Anastassiou, C.A., Koch, C., and Buzsáki, G. (2014). Theta phase segregation of input-specific gamma patterns in entorhinal-hippocampal networks. Neuron *84*, 470–485.

Séguinot, V., Maurer, R., and Etienne, A.S. (1993). Dead reckoning in a small mammal: the evaluation of distance. J. Comp. Physiol. A Neuroethol. Sens. Neural Behav. Physiol. *173*, 103–113.

Solstad, T., Solstad, T., Boccara, C.N., Boccara, C.N., Kropff, E., Kropff, E., Moser, M.-B., Moser, M.-B., Moser, E.I., and Moser, E.I. (2008). Representation of geometric borders in the entorhinal cortex. Science *322*, 1865–1868.

van Groen, T., Miettinen, P., and Kadish, I. (2003). The entorhinal cortex of the mouse: organization of the projection to the hippocampal formation. Hippocampus *13*, 133–149.

Vanderwolf, C.H. (1969). Hippocampal electrical activity and voluntary movement in the rat. Electroencephalogr. Clin. Neurophysiol. *26*, 407–418.

Vanderwolf, C.H. (1975). Neocortical and hippocampal activation relation to behavior: effects of atropine, eserine, phenothiazines, and amphetamine. J. Comp. Physiol. Psychol. *88*, 300–323.

Wells, C.E., Amos, D.P., Jeewajee, A., Douchamps, V., Rodgers, J., O'Keefe, J., Burgess, N., and Lever, C. (2013). Novelty and anxiolytic drugs dissociate two components of hippocampal theta in behaving rats. J. Neurosci. *33*, 8650–8667.

Wilson, M.A., and McNaughton, B.L. (1993). Dynamics of the hippocampal ensemble code for space. Science *261*, 1055–1058.

Wood, E.R., Dudchenko, P.A., Robitsek, R.J., and Eichenbaum, H. (2000). Hippocampal neurons encode information about different types of memory episodes occurring in the same location. Neuron *27*, 623–633.

Young, C.K., and McNaughton, N. (2009). Coupling of theta oscillations between anterior and posterior midline cortex and with the hippocampus in freely behaving rats. Cereb. Cortex *19*, 24–40.

Yu, J.Y., Kay, K., Liu, D.F., Grossrubatscher, I., Loback, A., Sosa, M., Chung, J.E., Karlsson, M.P., Larkin, M.C., and Frank, L.M. (2017). Distinct hippocampal-cortical memory representations for experiences associated with movement versus immobility. eLife *6*, 6.

Zheng, C., Bieri, K.W., Trettel, S.G., and Colgin, L.L. (2015). The relationship between gamma frequency and running speed differs for slow and fast gamma rhythms in freely behaving rats. Hippocampus *25*, 924–938.
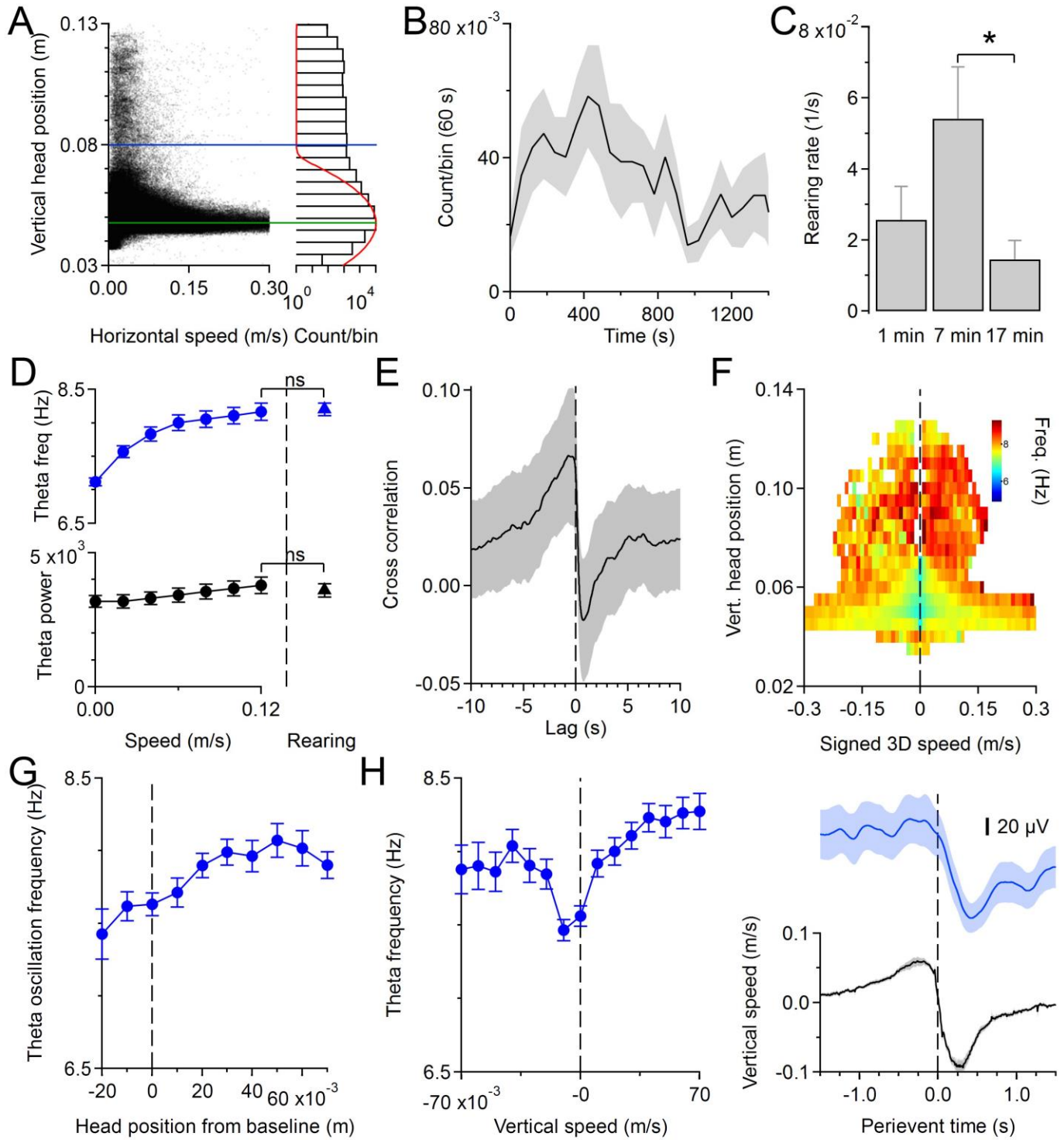
Supplemental Information

Hippocampal Network Dynamics

during Rearing Episodes

Albert M. Barth, Andor Domonkos, Antonio Fernandez-Ruiz, Tamas F. Freund, and Viktor Varga

Supplemental figures

Figure S1. Rearing events, related to figure 1. A) Detection of rearing events. Left: vertical head position plotted against horizontal running speed. Right: corresponding histogram of the vertical head positions. Red trace shows the fitted Gaussian curve (see Methods). Green line indicates the peak of the Gaussian curve, blue line denotes the threshold for rearing event detection. B) Time evolution of rearing incidence in open field (mean ± s.e.m, average n=12 animals). C) Rearing incidence reaches maximum around 7 min in open field (* p<0.05, n=12 animals, ANOVA with post-hoc Tukey HSD). D) Theta oscillation frequency and power increased with running speed but it was not significantly different from that is observed during rearing episodes (p>0.05, n=12 animals, paired t-test). E) Average cross-correlogram of the vertical head position vs high (7-12 Hz) theta oscillation power (mean ± s.e.m, n=12 animals). F) 3D speed-vertical head position 2D histogram from a representative animal. We rendered + or – sign to the 3D speed depending whether the head moved up- or downward. Note that higher theta frequencies appeared at higher 3D speeds at lower head positions and at lower upward 3D speeds at higher head positions. G) Summarized data of theta oscillation frequency as a function of vertical head position (Pearson's r = 0.32, p=0.002, n=12 animals). Note the flattening of the curve at higher head positions. Zero vertical head position indicates the baseline value (see: Supplemental Experimental Procedures). H) Summarized data show theta oscillation frequency depending on vertical head speed (*left*). Note the prominent dependence of theta oscillation frequency on upward vertical speed (Pearson's r for negative/downward speeds: -0.28, p=0.005, for positive/upward speeds: 0.51, p=1.1x10-7, n=12 mice). Vertical head speed starts to decrease before rearing peaks (*right bottom, black trace,* mean ± s.e.m, average n=12 animals) and the corresponding high theta magnitude also shows a decreasing tendency before rearing peak (*right top, blue trace,* mean ± s.e.m, average n=12 animals).
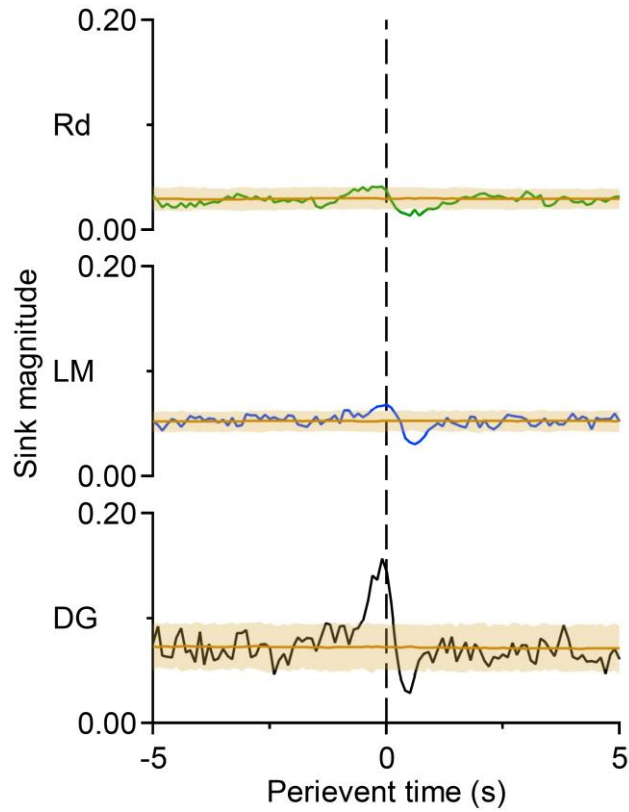
Figure S2. Perievent sink magnitude, related to figure 2. Rearing peak triggered magnitude of the 3 main sinks. Note the robust enhancement of the dentate sink. Brown traces indicate the shuffled control, shaded area represents the 99 % band of the shuffled control (*n=5* animals). Rd: radiatum, LM: lacunosum-moleculare, DG: dentate gyrus sinks.

A

30-50 Hz   50-100 Hz   120-150 Hz

Pr

Rd

LM

|50 μV |50 μV |10 μV

DG

-5   0   5   -5   0   5   -5   0   5
Perievent time (s) Perievent time (s) Perievent time (s)

B

-10   0   10
Perievent time (s)

C

0 s

0 360 720

0 360 720   0 360 720

-2 s   2 s

D

30-50 Hz   50-100 Hz   120-150 Hz

Pr   4 x10⁻³   9   3.5
                    x10⁻³   x10⁻³

Rd   4 x10⁻³   9   3.5
                    x10⁻³   x10⁻³

LM   4 x10⁻³   9   3.5
                    x10⁻³   x10⁻³

DG   4 x10⁻³   9   3.5
                    x10⁻³   x10⁻³

-5   0   5   -5   0   5   -5   0   5
Perievent time (s) Perievent time (s) Perievent time (s)

E

6 x10⁻³   ns

LM MI (50-100 Hz)

6 x10⁻³   *

DG MI (120-150 Hz)

0.00   0.06   0.12
Speed (m/s)   Rearing

F

30-50 Hz   50-100 Hz   120-150 Hz

Pr   8 x10⁻³   10   8
                    x10⁻³   x10⁻³

Rd   8 x10⁻³   10   8
                    x10⁻³   x10⁻³

LM   8 x10⁻³   10   8
                    x10⁻³   x10⁻³

DG   8 x10⁻³   10   8
                    x10⁻³   x10⁻³

-5   0   5   -5   0   5   -5   0   5
Perievent time (s) Perievent time (s) Perievent time (s)

G

10 x10⁻³   ns

LM CSD MI (50-100 Hz)

10 x10⁻³   *

DG CSD MI (120-150 Hz)

0.00   0.12
Speed (m/s)   Rearing

H

1000

700

400

100
5   10   15
Phase frequency (Hz)

Amplitude frequency (Hz)

2 x10⁻³

1

0

Figure S3. Gamma activity during rearing, related to figure 3. A) Average binned (bin size 1 s) rearing peak triggered perievent power in 3 different frequency bands and in different layers of the hippocampal formation. Note the tendency for mid and fast gamma increment around rearing peak. However, the layer specificity is distorted by volume conduction (brown traces indicate the shuffled control, shaded area represents the 99 % band of the shuffled control, $n=7$ animals). B) Sample perievent theta-gamma coupling values for fast gamma (120-150 Hz) at different depth of the hippocampal formation. Arrows indicate the robust enhancement of theta-gamma coupling around the rearing peak in the dentate gyrus. C) Sample theta-fast gamma phase amplitude histograms at 3 different time points around rearing peak. Black trace indicates vertical head position. D) Average perievent theta-gamma coupling values in 3 frequency bands and in the main layers of the hippocampal formation calculated from Hilbert magnitude values (brown traces indicate the shuffled control, shaded area represents the 99 % band of the shuffled control, $n=7$ animals). Note the prominent increment of theta-coupled fast gamma in the dentate gyrus. The mid gamma layer specificity is distorted by the presence of volume conduction. E) The coupling of LM mid gamma but not dentate fast gamma to theta oscillation increases with running speed (modulation index – running speed correlation Pearson's r for LM mid gamma: r=0.77, p<0.001; for dentate fast gamma: r=0.26, p > 0.1). However, rearing-coupled dentate theta – gamma coupling values were about 2 times as large as what was observed during running (* p<0.05, $n=7$ animals, paired t-test). F) Average perievent theta-gamma coupling values in 3 frequency bands and in the main layers of the hippocampal formation calculated from CSD traces (brown traces indicate the shuffled control, shaded area represents the 99 % band of the shuffled control, $n=5$ animals). G) The coupling of LM mid gamma and dentate fast gamma to theta oscillation increases with running speed calculated from CSD traces (modulation index – running speed correlation Pearson's r for LM mid gamma: r=0.61, p=0.001; for dentate fast gamma: r=0.46, p = 0.02). Note that dentate theta-fast gamma coupling values were about 2 times larger than that during running (* p<0.05, $n=5$ animals, paired t-test). H) Average crossfrequency-amplitude comodulogram for dentate gyrus LFP recordings. Note the restricted appearance of the theta dentate fast gamma coupling and the lack of CFC at higher, multiunit-contaminated frequencies (averages of $n=5$ animals). For A, D, F: Pr: pyramidal layer, Rd: radiatum, LM: lacunosum-moleculare, DG: dentate gyrus.

A

i

p

0.2 ms

Firing rate (Hz)

45

30

15

0

i

p

0   250   500 x10⁻⁶

Width at half max (s)

B

Count/bin

50 x10⁻³

0

50 x10⁻³

0

-0.1   0.0   0.1

Perievent time (s)

C

30 x10⁻³

Count/bin

0

30 x10⁻³

0

-100 x10⁻³   0   100

Perievent time (s)

D

Norm rearing num

1.0

0.5

0.0

Rel. vert. head pos. (m)

60 x10⁻³

30

0

-30

0.00   0.12

Distance from nearest wall (m)

E

Relative vert. head position (m)

60 x10⁻³

40

20

0

-20

0.00   0.04   0.08   0.12

Distance from nearest wall (m)

F

Normalized count/bin

0.15

0.00

0.81   0.77   0.84   0.79   0.9   0.74   0.43   0.63   0.94   0.8   0.79
1.85x10⁻⁵   6.68x10⁻⁵   4.48x10⁻⁶   3.29x10⁻⁵   8.17x10⁻⁸   1.81x10⁻⁴   0.06   2.64x10⁻³   1.55x10⁻⁹   2.68x10⁻⁵   3.55x10⁻⁵

0.15

0.00

0   360

Head Direction

Figure S4. Basic characteristics of separated units, related to figure 4. A) Sample putative interneuron (left top, i) and principal (left bottom, p) cell average waveforms registered in the CA1 pyramidal layer. Single units could be best separated based on their firing rate (right). Blue filled circles: place cells, red filled circles: rearing-ON units. Horizontal dashed line indicates the border between putative pyramidal and interneurons. Green "i" and "p" indicate the sample units on the left side. B) Autocorrelograms of a putative interneuron (*top*) and principal (*bottom*) cell (bin size = 1 ms). Cells are the same as in A. C) Rearing-ON units and place cells show increased activity during sharp wave ripples. Sample 150-250 Hz filtered LFP trace showing a sample ripple (top). Average ripple peak-triggered perievent histogram of rearing-ON units (middle, *n=6* units). Note that for the remaining 5 rearing-ON units there were not enough number of ripple events during the recording period. Average ripple peak-triggered perievent histogram of place cells (bottom, *n=12* units). D) 2D histograms present the border and vertical head position firing preference of rearing-ON units (*bottom*), above is the corresponding distribution of all rearing events from the nearest wall (*top*). Horizontal dashed line on the bottom diagrams indicates the threshold for rearing events. E) Average wall distance-vertical head position 2D histogram of the rearing-ON units (*n=11*). In D and E red-brown colors indicate higher normalized spike numbers. F) Head direction tuning of rearing-ON units. Histograms in grey present the observed head direction tuning of the rearing-ON units (*top*), below the corresponding horizontal position-based reconstructed (see Supplemental Experimental Procedures) tuning histograms (*bottom*, black histograms). Numbers in the middle indicate the corresponding Pearson's r (upper number) with the p value (lower number). Note the high correlation values between the observed and reconstructed tuning curves.

Table S1 related to figure 1. Summary table presenting details about the 12 mice involved in this study.

Animal ID	Genotype (C57Bl/6J)	Number of trials	Previous experience (min)	Dorsal hippocampus probe (NeuroNexus)	Number of rearing events	Analysis of spectral changes in low frequency bands	Analysis of LFP theta-gamma coupling	Analysis CSD	Analysis ICA	Analysis units
1957	Vgat-ires-Cre	1	33	A1x32-6/10mm-50-177	132	yes	yes	yes	yes	
1959	Vglut3-ires-Cre	1	0	Buzsaki32	74	yes				
1966	Som-ires-Cre	1	40	A1x32-6/10mm-50-177	45	yes	yes			
1969	Som-ires-Cre	1	0	A1x32-6/10mm-50-177	29	yes	yes			yes
1971	Som-ires-Cre	1	0	Buzsaki32	38	yes				yes
1977	Som-ires-Cre	1	45	A1x32-6/10mm-50-177	65	yes	yes	yes	yes	
1982	Som-ires-Cre	1	30	A4x16-6mm-50-703, A1x32-6/10mm-50-177	27	yes	yes	yes	yes	yes
1984	wild type	1	0	A1x16-6/10mm-100-177	84	yes	yes		yes	yes
1986	Som-ires-Cre	1	11	A4x16-6mm-50-703, A1x32-6/10mm-50-177	17	yes	yes	yes	yes	yes
1989	Som-ires-Cre	1	0	Buzsaki32	19	yes				yes
1991	Vglut3-ires-Cre	1	0	Buzsaki32	74	yes				yes
2089	wild type	3	0	A1x64-Poly2-6mm-23s-160	176	yes				yes

Only animals implanted with linear type silicone probes could be used for CSD and ICA analysis. In one animal the linear probe was located at the apex of the dentate gyrus, in two other animals there were several bad channels on the linear probe thus, recordings from these animals could not be used for reconstructing the CSD and ICA. In one other animal the linear probe was just above the granule cell layer therefore it could not be used for dentate CSD map analysis. Under the "previous experience" (4.) column we summarized the time each animal spent in the same arena within 5 days preceding the recordings.

Supplemental experimental procedures

CONTACT FOR REAGENT AND RESOURCE SHARING

Further information and requests for resources and reagents should be directed to and will be fulfilled by the Lead Contact, Viktor Varga (varga.viktor@koki.mta.hu).

RESOURCE TABLE

REAGENT or RESOURCE	SOURCE	IDENTIFIER
Experimental Models: Organisms/Strains		
Mice: C57Bl/6JCrl wild type	Inst. Exp. Med. own animal facility	N/A
Mice: vGLUT3-ires-Cre	The Jackson Laboratory	https://www.jax.org/strain/018147
Mice: SOM-ires-Cre	The Jackson Laboratory	https://www.jax.org/strain/013044
Mice: vGAT-ires-cre	The Jackson Laboratory	https://www.jax.org/strain/016962
Software and Algorithms		
MATLAB	MathWorks	**RRID:SCR_001622**
SpikeDetekt	Rossant et al., 2016	https://github.com/klusta-team/spikedetekt
KlustaKwik	Rossant et al., 2016	**RRID:SCR_014480**
KlustaViewa	Rossant et al., 2016	https://github.com/klusta-team/klustaviewa/)
Spyking Circus	Yger et al., 2016	https://github.com/spyking-circus/spyking-circus
Phy	http://phy-contrib.readthedocs.io/en/latest/template-gui/	https://github.com/kwikteam/phy
ICA algorithms	EEGLAB	https://sccn.ucsd.edu/eeglab/
Igor Pro7	Wavemetrics Inc	**RRID:SCR_000325**
OptiTrack	NaturalPoint Inc	http://optitrack.com/software/
Other		
Silicone probe: 32-sites, 4-shank probe	NeuroNexus	Buzsaki32
Silicone probe: 32-sites, 1-shank probe	NeuroNexus	A1x32-6mm-50-177
Silicone probe: 64-sites, 4-shank probe	NeuroNexus	A4x16-5mm-50-500-703
Silicone probe: 64-sites, 1-shank probe	NeuroNexus	A1x64-Poly2-6mm-23s-160
256 channel Multiplexed Biosignal Amplifier	Amplipex	http://www.amplipex.com/products/large-scalerecording/?single_prod_id=37

METHODS DETAILS

Animal surgery

Animals were anesthetized with isoflurane anesthesia and mounted in the stereotaxic frame (David Kopf Instruments, Tujunga, CA). The cranium was exposed and one or several craniotomies were performed under stereotaxic guidance. Linear or Buzsaki32 type silicon probes (Table S1, NeuroNexus, Ann-Arbor, MI) were implanted in the dorsal hippocampus. The probes were fixed on custom-made micro-drives attached to the skull with dental acrylate. The craniotomies were sealed with artificial dura (Cambridge NeuroTech Ltd, Cambridge, UK). Two stainless steel screws placed above the cerebellum served as ground and reference for the recordings.

The probe-microdrive ensemble was shielded by a copper mesh preventing the contamination of the recordings by environmental electric noise. Following the surgery, the animals were continuously monitored until recovered as demonstrated by their ability to exhibit purposeful movement. After post-surgery recovery, the probes were moved gradually by the custom-made microdrive in 75 to 150 µm steps per day until the target area was reached.

The pyramidal layer in the CA1 region was identified physiologically by increased unit activity and the occurrence of ripple activity. The identification of CA1 and dentate gyrus layers was achieved by the application of current source density and independent component analysis to the local field potentials (Fernández-Ruiz and Herreras, 2013; Fernández-Ruiz et al., 2012) and by characteristic physiological markers such as the reversal of sharp-waves and depth profile of theta oscillation amplitude.

Data acquisition

Animals were placed in a rectangular arena (60 x 60 cm, 20 cm wall height) to allow spontaneous open field exploratory behavior. The arena walls and floor were made of grey plastic. Specific extra-box cues were not used, however from the arena the animals could see the experimental room. Some animals used in this study already had previous experience in the same arena within 5 days before recordings (see Table S1).

Electrophysiological recordings were performed by connecting the implanted silicone probe to a signal multiplexing headstage attached to a flexible lightweight cable. Electrophysiological signals were acquired at 20k sample/s (KJE-1001, Amplipex Ltd, Hungary).

The movement of the animal was tracked by an infrared marker-based high speed (120 frame / sec) 4-camera (Flex13, NaturalPoint, Inc., Corvallis, OR) motion capture system capable of reconstructing the animal's position and orientation in 3 dimensions with submillimeter resolution (Motive, OptiTrack, NaturalPoint, Inc., Corvallis, OR). The infrared-reflective markers (3 mm diameter hemispheres) were attached to the head-assembly of the mice or to the headstage.

Tissue processing

Following the termination of the experiments, animals were deeply anesthetized and transcardially perfused first with 0.9% saline solution followed by 4% paraformaldehyde solution. Brains were sectioned in 60-µm thick slices (Leica Biosystems, Wetzlar, DE). Probe tracks were reconstructed on the consecutive tissue slices.

Detection of rearing events

A histogram of all sampled vertical head positions was generated and a Gaussian was fitted to the left part of the histogram not skewed by rearing events. The mean of the fitted Gaussian was considered to be the mean baseline head position. Vertical headposition bin where the fitted Gaussian returned to 0 was defined as rearing threshold (Figure S1A).

Validation of rearing definition

To validate our rearing definition, we carried out further experiments to investigate the forelimb position relative to the ground and the vertical head position. We glued a mock head assembly with infrared markers and headstage connectors to the head of 3 mice, but without implanting electrodes. From the three mice one exhibited enough rearing events. The size and shape of the „dummy" headmounts were similar to those with electrodes used in this study. The camera configuration of the 3D tracking system was modified: one of the four top mounted cameras was placed at the ground level of the open field arena to provide side view of the animal. The wall of the arena in front of the side camera was removed. By elevating the floor, we created a 5 cm drop to prevent escape from the arena. The height of the sideview camera was adjusted to show the horizontal line of the ground plane. During tracking we connected the animal to the cable the same way as during electrophysiological recordings but only tracking data was registered. Tracking data and sideview video were offline analyzed. The videos were manually analyzed by looking for frames corresponding to the moment when both paws detached from the arena floor. We paired these frames with the tracking data to find vertical head positions corresponding to the release of the floor. Vertical head positions were measured relative to the mean baseline head position. We found that the vertical head position at the moment of paw detachment is, on average 34.8 ± 3.0 mm. This value is very close to the average rearing threshold used in this study: 34.4 ± 2.6 mm.

Time-frequency analysis

To analyze oscillatory activity during rearing events we obtained the Morlet wavelet decomposition or Hilbert transformation of the LFP recordings. The Hilbert magnitudes of different frequency bands were averaged by triggering on rearing peaks. Shuffled averages were generated for each frequency band by randomly selecting timepoints in the 20 s interval (10 s before, 10 s after) around each rearing peak repeated by 1000 times. The perievent average traces were plotted with the corresponding 99% confidence bounds of the shuffled data. If the average trace exceeded the 99% confidence bounds at least for 0.5 s (> 5% of rearing event duration) during rearing event, we defined as significant alterations. We further verified the significance of the alterations by comparing values during rearing and baseline periods (5-10 s before rearing peak). We performed the above shuffling procedure, and applied the same criteria of significance for perievent modulation indices calculations (see Figure 3H and Figure S3D,F).

We defined the onset of the significant alteration (for Figure H) when the perievent average trace crossed the 95 % confidence bound of the shuffled control for at least 0.2 s.

Cross-correlation analysis

Time lag between change of vertical head position and alteration of power in the high theta band was calculated from their cross-correlogram (CCG). First, both time series were downsampled to 100 Hz and their mean was subtracted. Then, the CCG was computed by Igor Pro's built-in cross-correlation function. The time of the CCG's positive peak corresponded to the time lag between the two time series.

Current source density analysis

To produce current source density (CSD) estimates the second spatial derivatives of the voltage profile were calculated (Nicholson and Freeman, 1975). To calculate CSD during rearing the second spatial derivatives were averaged around theta cycle peaks closest to rearing peaks. For CSD analysis during running episodes, segments when movement speed was above 4 cm/s were used.

Independent Component Analysis of LFPs

To address the inverse problem of LFPs, that is, to separate the different sources that contribute to the mixed signal, we employed a combination of independent component analysis (ICA) and current source density (CSD) analysis as had been described and validated previously (Fernández-Ruiz and Herreras, 2013; Fernández-Ruiz et al., 2012).

ICA is a blind source-separation technique (Bell and Sejnowski, 1995; Comon, 1994) that can isolate spatially segregated stable patterns of activity in a mixed signal recorded with an array of sensors. Applied to linear profiles of LFPs it can separate physiologically meaningful sources that can be attributed to known anatomical pathways, as has been demonstrated for the CA1, CA3 and dentate regions of the rat hippocampus (Benito et al., 2014; Fernández-Ruiz and Herreras, 2013; Fernández-Ruiz et al., 2012).

Here, we applied ICA to spatially contiguous LFP channels along the dorso-ventral hippocampal axis. The algorithm takes a time series of data with dimension equal to the number of recording sites, and returns a time series of the same dimensionality, but rotated such at each dimension to represent a different IC. The inverse of the mixing matrix that transforms the LFP data into the ICs gives the channel weight of each component that is captured for each electrode. When plotted according to the anatomical location of the electrodes, this corresponds to the spatial voltage loadings of each IC (Fernández-Ruiz et al., 2012). Once ICs have been extracted from the raw LFP traces, they can be analyzed as if they were active independently from activities at other locations.

The optimization of ICA of LFPs for high-frequency activity require a series of pre-processing steps that have been described in detail elsewhere (Fernández-Ruiz et al., 2017; Schomburg et al., 2014).

Cross-Frequency Coupling of LFPs

Theta-band phase of the LFP recorded in CA1 pyramidal layer was calculated by Hilbert transformation of the 5-12 Hz bandpass filtered LFP. Theta epochs were detected where the animals' running speed exceeded 4 cm/s for 2 s. Theta peaks correspond to 180° and troughs to 0° and 360° of theta waves recorded in the CA1 pyramidal layer throughout the manuscript.

To analyze high-frequency oscillatory activity in the LFP at a high resolution in time and frequency, the continuous wavelet transform (CWT) of the LFP (or ICs) was calculated using complex Morlet wavelets (Torrence and Compo,

1998). The phase-amplitude cross-frequency coupling (CFC) during theta oscillations for a given LFP recording was assessed using the modulation index (MI) (Tort et al., 2010). Wavelet phase was calculated at 100 levels from 0.2-20 Hz, and the amplitude at 170 levels from 30-200 Hz. Phase time-series were binned into phase intervals and the mean wavelet amplitude was calculated for each of them (Fernández-Ruiz et al., 2017). The MI was obtained by measuring the divergence of the observed amplitude distribution from the uniform distribution. The statistical significance of the MI values was assessed by a surrogate analysis (n = 500 surrogates) with random shifts between the phase and amplitude time series (Canolty et al., 2006).

All LFP analysis was performed with custom-made MATLAB (The MathWorks, Inc., Natick, MA) and IgorPro7 (Wavemetrics, Lake Oswego, OR) scripts available upon request.

Spike sorting

Neuronal spikes were detected and automatically sorted from the high-pass filtered LFP (0.5–5 kHz) either by the masked EM or by a template matching algorithm (KlustaKwik (Rossant et al., 2016) or Spyking-Circus (Yger et al., 2016) followed by manual adjustment of the clusters using the KlustaViewa or Phy softwares (Rossant et al., 2016) to obtain well-isolated single units. Cluster isolation quality was estimated by calculating the interspike interval index for each cluster (Schmitzer-Torbert et al., 2005); poor quality clusters were discarded.

Putative pyramidal cells and interneurons were separated on the basis of their firing rate, spike width and autocorrelograms (Csicsvari et al., 1998).

Definition of rearing-ON units and place cells

All place cells and rearing-ON units were identified as putative principal units in the CA1 pyramidal layer of the dorsal hippocampus. The rearing-ON units were defined based on their rearing peak triggered perievent histograms. Shuffled control perievent histograms were created based on randomly selecting timepoints within a 20 s window of each rearing event. The observed and shuffled control perievent histograms were compared (Wilcoxon-Mann-Whitney-test) and if there were significant firing increment around rearing peaks (-0.25 and +0.25 s) the unit was defined as rearing-ON units. Place cells were defined based on their 2D firing rate map. The arena was divided into 2 x 2 cm spatial bins. The dwell time normalized firing rate was calculated in each spatial bin. Place field was defined as at least 5 continuous spatial bins where the firing rates were above the mean firing rate + at least 2 standard deviations. A place cell was defined if it had at least one place field and the corresponding spatial information was above 0.5. Rate map, spatial information and sparsity were calculated as previously described (Skaggs et al., 1996). Place fields with fewer than 50 spikes were discarded.

Activity of rearing-ON units

The average rearing peak-triggered perievent histogram of rearing-ON units indicate robust enhancement around rearing peaks. However, rearing-ON units show elevated activity only in a subset of rearing events ("active" rearing events for that rearing-ON units). A baseline firing rate was calculated 5 – 10 s before each rearing peak and active rearing events

were defined when the firing rate exceeded the baseline firing rate with 1 standard deviation in a 1 s window around the rearing peak.

We further investigated the spatial dispersion of these active rearing events for each rearing-ON unit (i.e. rearing events with associated ON unit activation, shortly active events). As a null hypothesis we assumed that the spatial dispersion of active events, namely the average distance between any two active events is equal to the distance of any two randomly selected rearing events (independent of their association with ON unit activation). To test against the null hypothesis first for each rearing-ON unit, rearing events were randomly selected to get an equal quantity to the number of active events. Then the average horizontal distance among the spatial location of the selected events was calculated and compared to the mean distance among active events. The random selection and the corresponding average distance calculation was repeated 100 times.

The spatial distribution of active events was further analyzed by calculating their distance from the walls and defining a distance threshold of 5 cm based on which all rearing episodes were divided into peripheral and central events and the proportion of active events in these categories was determined.

Reconstruction of head direction curves

To investigate the head direction tuning of rearing-ON units it is important to analyze the effect of behavioral constrains which can result in apparent head direction tuning. The effect of behavioral constrains can be especially important at rearing related activity. We found that rearing events mostly occurred at the periphery where the animal preferentially faced toward the wall. To avoid this behavioral "bias" we followed previous reports to calculate reconstructed head direction tuning curves (Muller et al., 1994; Rubin et al., 2014). By comparing the observed and reconstructed head direction curves we tested whether head-direction tuning curves of the rearing-ON units could be a byproduct of the location of the firing locations.

DATA AND SOFTWARE AVAILABILITY

Data included and software used in this article will be available upon request.

Supplemental references

Bell, A.J., and Sejnowski, T.J. (1995). An information-maximization approach to blind separation and blind deconvolution. Neural Comput. *7*, 1129–1159.

Benito, N., Fernández-Ruiz, A., Makarov, V.A., Makarova, J., Korovaichuk, A., and Herreras, O. (2014). Spatial modules of coherent activity in pathway-specific lfps in the hippocampus reflect topology and different modes of presynaptic synchronization. Cereb. Cortex *24*, 1738–1752.

Canolty, R.T., Edwards, E., Dalal, S.S., Soltani, M., Nagarajan, S.S., Kirsch, H.E., Berger, M.S., Barbaro, N.M., and Knight, R.T. (2006). High gamma power is phase-locked to theta oscillations in human neocortex. Science *313*, 1626–1628.

Comon, P. (1994). Independent component analysis, A new concept? Signal Processing *36*, 287–314.

Csicsvari, J., Hirase, H., Czurko, A., and Buzsáki, G. (1998). Reliability and state dependence of pyramidal cell-interneuron synapses in the hippocampus: An ensemble approach in the behaving rat. Neuron *21*, 179–189.

Fernández-Ruiz, A., and Herreras, O. (2013). Identifying the synaptic origin of ongoing neuronal oscillations through spatial discrimination of electric fields. Front. Comput. Neurosci. *7*, 5.

Fernández-Ruiz, A., Makarov, V.A., and Herreras, O. (2012). Sustained increase of spontaneous input and spike transfer in the CA3-CA1 pathway following long-term potentiation in vivo. Front. Neural Circuits *6*, 71.

Fernández-Ruiz, A., Oliva, A., Nagy, G.A., Maurer, A.P., Berényi, A., and Buzsáki, G. (2017). Entorhinal-CA3 Dual-Input Control of Spike Timing in the Hippocampus by Theta-Gamma Coupling. Neuron *93*, 1213–1226.e5.

Muller, R.U., Bostock, E., Taube, J.S., and Kubie, J.L. (1994). On the directional firing properties of hippocampal place cells. J. Neurosci. *14*, 7235–7251.

Nicholson, C., and Freeman, J.A. (1975). Theory of current source-density analysis and determination of conductivity tensor for anuran cerebellum. J. Neurophysiol. *38*, 356–368.

Rossant, C., Kadir, S.N., Goodman, D.F.M., Schulman, J., Hunter, M.L.D., Saleem, A.B., Grosmark, A., Belluscio, M., Denfield, G.H., Ecker, A.S., et al. (2016). Spike sorting for large, dense electrode arrays. Nat. Neurosci. *19*, 634–641.

Rubin, A., Yartsev, M.M., and Ulanovsky, N. (2014). Encoding of Head Direction by Hippocampal Place Cells in Bats. J. Neurosci. *34*, 1067–1080.

Schmitzer-Torbert, N., Jackson, J., Henze, D., Harris, K., and Redish, A.D. (2005). Quantitative measures of cluster quality for use in extracellular recordings. Neuroscience *131*, 1–11.

Schomburg, E.W., Fernández-Ruiz, A., Mizuseki, K., Berényi, A., Anastassiou, C.A., Koch, C., and Buzsáki, G. (2014). Theta Phase Segregation of Input-Specific Gamma Patterns in Entorhinal-Hippocampal Networks. Neuron *84*, 470–485.

Skaggs, W.E., McNaughton, B.L., Wilson, M.A., and Barnes, C.A. (1996). Theta phase precession in hippocampal neuronal populations and the compression of temporal sequences. Hippocampus *6*, 149–172.

Torrence, C., and Compo, G.P. (1998). A Practical Guide to Wavelet Analysis. Bull. Am. Meteorol. Soc. *79*, 61–78.

Tort, A.B.L., Komorowski, R., Eichenbaum, H., and Kopell, N. (2010). Measuring Phase-Amplitude Coupling Between Neuronal Oscillations of Different Frequencies. J. Neurophysiol. *104*, 1195–1210.

Yger, P., Spampinato, G.L.B., and Esposito, E. (2016). Fast and accurate spike sorting in vitro and in vivo for up to thousands of electrodes. bioRxiv 1–21.